Radiative Transfer Modeling for the CLAMS Experiment

ZHONGHAI JIN,* THOMAS P. CHARLOCK,[+] KEN RUTLEDGE,* GLENN COTA,[#] RALPH KAHN,[@]
JENS REDEMANN,[&] TAIPING ZHANG,* DAVID A. RUTAN,* AND FRED ROSE*

*Analytical Services and Materials, Inc., Hampton, Virginia
[+]Atmospheric Sciences Division, NASA Langley Research Center, Hampton, Virginia
[#]Center for Coastal Physical Oceanography, Old Dominion University, Norfolk, Virginia
[@]Jet Propulsion Laboratory, California Institute of Technology, Pasadena, California
[&]Bay Area Environmental Research Institute, Sonoma, California

ABSTRACT

Spectral and broadband radiances and irradiances (fluxes) were measured from surface, airborne, and space-borne platforms in the Chesapeake Lighthouse and Aircraft Measurements for Satellites (CLAMS) campaign. The radiation data obtained on the 4 clear days over ocean during CLAMS are analyzed here with the Coupled Ocean–Atmosphere Radiative Transfer (COART) model. The model is successively compared with observations of broadband fluxes and albedos near the ocean surface from the Clouds and the Earth's Radiant Energy System (CERES) Ocean Validation Experiment (COVE) sea platform and a low-level OV-10 aircraft, of near-surface spectral albedos from COVE and OV-10, of broadband radiances at multiple angles and inferred top-of-atmosphere (TOA) fluxes from CERES, and of spectral radiances at multiple angles from Airborne Multiangle Imaging Spectroradiometer (MISR), or "AirMISR," at 20-km altitude. The radiation measurements from different platforms are shown to be consistent with each other and with model results. The discrepancies between the model and observations at the surface are less than 10 W m^{-2} for downwelling and 2 W m^{-2} for upwelling fluxes. The model–observation discrepancies for shortwave ocean albedo are less than 8%; some discrepancies in spectral albedo are larger but less than 20%. The discrepancies between low-altitude aircraft and surface measurements are somewhat larger than those between the model and the surface measurements; the former are due to the effects of differences in height, aircraft pitch and roll, and the noise of spatial and temporal variations of atmospheric and oceanic properties. The discrepancy between the model and the CERES observations for the upwelling radiance is 5.9% for all angles; this is reduced to 4.9% if observations within 15° of the sun-glint angle are excluded.

The measurements and model agree on the principal impacts that ocean optical properties have on upwelling radiation at low levels in the atmosphere. Wind-driven surface roughness significantly affects the upwelling radiances measured by aircraft and satellites at small sun-glint angles, especially in the near-infrared channel of MISR. Intercomparisons of various measurements and the model show that most of the radiation observations in CLAMS are robust, and that the coupled radiative transfer model used here accurately treats scattering and absorption processes in both the air and the water.

1. Introduction

The Clouds and Earth's Radiant Energy System (CERES) sensor, the Multiangle Imaging Spectroradiometer (MISR), and the Moderate Resolution Imaging Spectroradiometer (MODIS) fly on board the National Aeronautics and Space Administration's (NASA) Earth Observing System (EOS) *Terra* satellite. CERES data are processed with MODIS inputs to yield an accurate, long-term atmospheric broadband radiation energy budget for studying the earth's climate. One application of MISR multiangle data is the retrieval of aerosol physical and optical properties. To develop and validate the retrieval algorithms for aerosol, surface fluxes, and radiative forcing from CERES, MODIS, and MISR observations, a field campaign, the Chesapeake Lighthouse and Aircraft Measurements for Satellites (CLAMS), was conducted over the Atlantic Ocean off Virginia Beach, Virginia, during the summer of 2001. CLAMS is primarily a shortwave radiative closure experiment. Downwelling and upwelling spectral and broadband radiance and irradiance (flux) were measured from aircraft, from a rigid platform (the Chesapeake lighthouse tower), and from *Terra* during CLAMS (10 July–2 August 2001). Comprehensive observations of atmospheric and oceanic properties, which affect radiative transfer processes, were also conducted during CLAMS. In this paper, we present only those radiation data measured over the ocean in 4 clear days in CLAMS and analyze them with

Corresponding author address: Dr. Zhonghai Jin, Analytical Services and Materials, Inc., 1 Enterprise Parkway, Suite 300, Hampton, VA 23666.
E-mail: z.jin@larc.nasa.gov

the Coupled Ocean Atmosphere Radiative Transfer (COART) model (Jin et al. 2002). A detailed description of all measurements in the CLAMS experiment is given in Smith et al. (2005).

Section 2 briefly describes the radiation measurements to be studied and the relevant optical properties of the atmosphere and ocean used as inputs to the radiative transfer model. Section 3 briefly describes the model used. Section 4 analyses and compares the radiation measurements from aircraft, surface, satellite, and modeling. Finally, the summary and conclusions are given in section 5.

2. Measurements of radiation and optical properties in the atmosphere and ocean

Several instrumented aircraft from different agencies in the United States participated in the CLAMS campaign to measure optical properties of the atmosphere and ocean in the vicinity of the CERES Ocean Validation Experiment (COVE) site and over the surrounding ocean, nearby National Oceanic and Atmospheric Administration (NOAA) buoys, and a few coastal land sites. The COVE ocean platform is the focus of the CLAMS experiment and is an important validation site for CERES's Surface and Atmospheric Radiation Budget (SARB) flux profile retrievals (Charlock and Alberta 1996). This study focuses on radiation data obtained on 4 clear days during CLAMS in the vicinity of COVE. The radiation measurements and relevant ancillary atmospheric and oceanic property observations used as model input are described briefly in this section.

In CLAMS, the NASA Langley Research Center's OV-10 aircraft measured the broadband downwelling and upwelling irradiances with Eppley model Precision Spectral Pyranometers (PSP) and spectral irradiances with Analytical Spectral Devices (ASD) spectrometers over the spectral range 350–2200 nm at resolutions of 3–10 nm.

The Airborne MISR (AirMISR) instrument on board the NASA high-altitude ER-2 aircraft measured upwelling radiances 20 km above the surface in four spectral bands centered at 446, 558, 672, and 867 nm for each of nine view angles spread out in the forward and aft directions along the flight paths at $\pm70.5°$, $\pm60.0°$, $\pm45.6°$, $\pm26.1°$, and nadir (Kahn et al. 2001; Diner et al. 1998).

Surface measurements were based at the Chesapeake lighthouse ocean platform (COVE), which is 25 km east of the coast of Virginia at the mouth of the Chesapeake Bay. Broadband upwelling flux at the surface was measured by an Eppley model PSP. The PSP was installed at the end of a frame displaced horizontally 6.7 m from the main platform and vertically 21.3 m above the sea surface. Broadband direct solar insolation was measured by a Kipp and Zonen (KZ) model CH1 pyrheliometer; downwelling diffuse and global fluxes were measured by shaded and unshaded pyranometers (KZ model

CM31), respectively. Narrowband upwelling and downwelling fluxes were measured by multifilter rotating shadowband radiometers (MFRSR) at six channels in the visible and near-infrared spectrum. The MFRSR for spectral upwelling flux was collocated with the PSP for broadband upwelling flux. The downwelling spectral irradiance was also measured at COVE by the ASD spectrometer.

A number of ancillary measurements were made at COVE during the CLAMS experiment. Those relevant to this study include aerosol properties, profiles of atmospheric pressure, temperature, humidity (water vapor density), wind speed, ocean surface status, and ocean optics. Radiosondes for atmospheric profiles were launched from COVE at 0000, at 1200 UTC, near *Terra* overpass time (roughly at 1600 UTC), and at other times coinciding with selected aircraft measurements. Integrated precipitable water (PW) was measured using a dual-frequency Global Positioning System (GPS) instrument by NOAA's GPS demonstration network. NOAA's meteorology station at COVE routinely measured standard meteorological parameters (wind, temperature, pressure, humidity, etc.). COVE is also a site for the Aerosol Robotic Network (AERONET; Holben et al. 1998), which is a federation of ground-based remote sensing aerosol networks. AERONET measured aerosol spectral optical depths using Cimel sun photometers; the data were inverted to obtain other aerosol optical properties (Dubovik and King 2000). The Cimel sun photometer made periodic almucantar and solar principal plane atmospheric radiance scans to determine aerosol scattering phase function and particle size distribution. The 14-channel NASA Ames Airborne Tracking Sunphotometers (AATS-14) on the University of Washington (UW) Convair-580 aircraft also measured aerosol optical depth (AOD) at 13 wavelengths from 354 to 1558 nm from various altitudes (Redemann et al. 2005).

Oceanographic observations were made at COVE by a team from the Old Dominion University (ODU) to measure chlorophyll concentration (Chl) and absorption coefficients of soluble colored dissolved organic materials (CDOM) and particulate (phytoplankton and nonpigmented) materials in the water twice per day. Depth profiles of temperature and salinity were also measured.

3. Description of radiative transfer model

In this study, we use the COART radiative transfer model for radiance and irradiance (flux) calculations (Jin et al. 2002). COART is evolved from the coupled atmosphere–ocean radiative transfer model developed by Jin and Stamnes (1994) and is based on the Coupled Discrete Ordinate Radiative Transfer (CDISORT) code. The CDISORT is developed from DISORT (Stamnes et al. 1988), a publicly distributed software tool for radiative transfer. DISORT, which has been widely used in the atmospheric sciences community, treats the sur-

face (land or ocean) as a fixed boundary condition, hence radiative transfer models based on DISORT compute nothing beneath the ocean surface. However, it is well known that the optical properties within the ocean affect the upwelling radiation to the atmosphere; and that the optical properties of the atmosphere affect the radiation penetrating into the ocean. In other words, the radiation fields in the atmosphere and in the ocean interact with each other. Therefore, it is more consistent to treat the radiative transfer process in the atmosphere and ocean as a coupled system. This consistent (coupled) solution requires the refractive index variation at the air–water interface to be taken into account: this index variation causes reflection and refraction at the air–water interface to differ from that at the interfaces between atmospheric layers. Due to the inclusion of a new variable (i.e., the refractive index) in the radiative transfer equation, the formulation and solution of the equation are different from those for radiative transfer problems in the atmosphere alone. The detailed formulation and solution of the radiative transfer equations in the coupled atmosphere–ocean system using the discrete ordinate method was given by Jin and Stamnes (1994) and is not repeated here. This solution was also confirmed by a comparison with six similar models implemented by different algorithms, mostly by Monte Carlo method (Mobley et al. 1993).

However, the solution presented in Jin and Stamnes (1994) is for the flat ocean surface. Calm ocean conditions are very rare. The wind roughens the ocean, thereby affecting the reflection and transmission of the incident radiation at the surface, and subsequently the albedo, solar heating within the ocean, and the pattern of sun glint. Introducing the ocean surface roughness into the radiative transfer equation further complicates the solution. We recently included the windblown ocean surface roughness analytically in the solution using the Cox and Munk (1954) surface slope distribution, which is a function of wind speed (Jin et al. 2002).

Because the radiative transfer equations now include the refractive index and the windblown ocean surface roughness effect, our solution for the coupled atmosphere–ocean system becomes consistent and rigorous. This feature enables COART to consider ocean layers as just additional "atmospheric layers" but with greatly different optical properties. COART treats absorption and scattering processes in the atmosphere and ocean explicitly. These include the scattering and absorption by atmospheric molecules, aerosols, and clouds in the atmosphere, and by water molecules, soluble (e.g., CDOM) and particulate (e.g., phytoplankton particles) materials in the ocean. Optical properties of aerosol and clouds in the atmosphere and of particulate and soluble materials in the ocean for model input can be from measurement data, if available, or from parameterizations via relevant physical properties.

Unlike most radiative transfer schemes, COART has options for separate treatment of detailed narrowband and fast broadband computations. The narrowband scheme is designed for spectral or narrowband radiance and irradiance calculations, in which users can specify an arbitrary wavelength or spectral range. In this scheme, COART adopts the Low-Resolution Transmittance–7 (LOWTRAN 7) band model and its molecular absorption database for atmosphere, which has a spectral resolution of 20 cm^{-1}. This is equivalent to a wavelength resolution of about 0.5 nm at 500-nm wavelength and 8 nm at 2000 nm. However, a calculation of the total radiance or irradiance over a wide spectral range by integration of narrowband results is computationally too expensive. To overcome this difficulty, we usually divide the solar spectrum into some fixed set of wavelength intervals and use an averaged atmospheric transmissivity in each interval computed from the line-by-line code monochromatic results. For broadband calculations, COART uses 26 fixed wavelength intervals in the solar spectrum considered (0.20–4.0 μm). In each spectral interval, the average transmissivity is obtained by the popular k-distribution method (Kato et al. 1999), in which, molecular absorption by all atmospheric gases (mainly H_2O, CO_2, O_3, and O_2 for solar radiation) is based on the new high-resolution transmission molecular absorption (HITRAN) 2000 database.

4. Data presentation and analysis

a. Atmospheric and oceanic parameters measured for model input

In addition to radiation measurements, CLAMS also made comprehensive measurements of the physical and optical properties of the atmosphere and ocean at and around COVE. Our model simulations and data analyses focus on 4 clear days during CLAMS (17 July, 31 July, 1 August, and 2 August 2001). This subsection describes the measurements of the most relevant model input parameters for these days.

Figure 1 shows temperature and water vapor profile soundings at COVE on the 4 days, near *Terra* overpass time. The 8-digit numbers represent the sounding time as month, day, UTC time, and minute. Figure 2 presents the total PW from GPS and wind speed measured by NOAA's instruments at COVE as a function of UTC time for the same days. NASA Cimel instrument at COVE provides AOD at seven wavelengths (340, 380, 440, 500, 670, 870, and 1020 nm) and single scattering albedo (SSA) at four wavelengths (441, 673, 873, and 1022 nm). Figure 3 shows the measured AOD (500 nm) and SSA (673 nm) each at one wavelength, indicating that the aerosol loading is much larger on 7/17 than on other days. Aerosol scattering phase functions are also available from AERONET at four wavelengths, but temporal coverage is sparse.

Some ocean parameters were measured in situ during CLAMS. Figure 4 shows averages of the spectral absorption coefficients measured at COVE during CLAMS
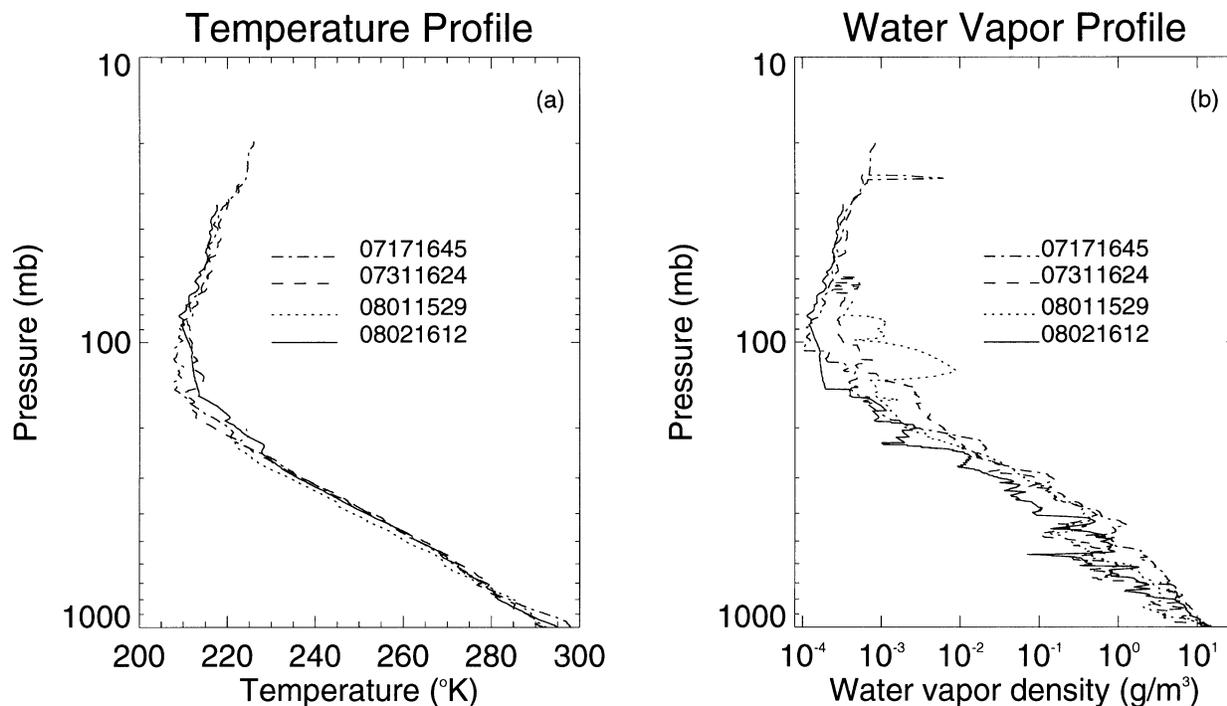
FIG. 1. The (a) temperature and (b) water vapor profiles measured at COVE on the 4 clear days during CLAMS. The 8-digit numbers represent the sounding time in order of month, day, UTC time, and minute.

for CDOM (which is soluble, rather than particulate), phytoplankton (a subset of the particulate matter) and all particles. These measurements indicate that the absorption from ocean materials (other than H_2O) at COVE is dominated by CDOM for wavelengths less than 400 nm, while it is mainly contributed by particulates for wavelengths longer than 600 nm. There are 87 measurements of chlorophyll concentration in CLAMS. Chlorophyll indicates the phytoplankton biomass in seawater and is the principal parameter used in bio-optical models to parameterize the absorption and scattering by ocean particles (Morel 1991). The mean measured chlorophyll concentration in surface waters at COVE is 1.33 mg m^{-3}, while a standard deviation of 0.9 mg m^{-3} demonstrates substantial variability. The absorption peaks of chlorophyll at around 440 and 670 nm are seen in the absorption spectrum for phytoplankton presented in Fig. 4. All these atmospheric and oceanic properties measured at the corresponding times are used in model simulations of radiation in the following section.

b. Comparisons between measurements and model

1) BROADBAND SHORTWAVE

Figure 5 shows the NASA OV-10 aircraft flight tracks with special low-altitude (183 and 31 m) measurements of broadband fluxes during the 4 clear days at CLAMS. The circle represents the location of the Chesapeake Lighthouse—the COVE site (36.905°N, −75.713°E)—

which is also the center of the CLAMS experiment domain. Each of the five panels (Fig. 5) represents a series of flight legs over the ocean, and each solid line represents the level portion of a flight leg. There were two flights, each with a distinct panel, on 2 August 2001. Corresponding to the flight legs in each panel in Fig. 5, Fig. 6 compares the measured and modeled downward shortwave fluxes (irradiances). Figure 6 includes fluxes for the COVE platform, as well as for the aircraft: Figs. 6a1–6a5 show the fluxes themselves; Figs. 6b1–6b5 show the respective differences of aircraft and surface (COVE) measurements, and then the differences of the model and surface measurements. Most aircraft data were taken 183 m above the ocean; a few legs were at 31 m. Figures 6a1 to 6a5 and Figs. 6b1 to 6b5 correspond with the five panels in Fig. 5, respectively. The abscissa in Fig. 6 gives the flight time in UTC and each section of the solid lines corresponds in time to a flight leg in the respective panel in Fig. 5. The aircraft data (red lines in Figs. 6a1 to 6a5) are averaged for each leg. The dashed–dotted lines in Fig. 6 are model results based on the input parameters described in section 4a. To remove the solar zenith dependence, results in each panel are normalized to the solar zenith at the start of each flight series. The effects of changing solar zenith angle are small here, except for flight 2 on 2 August (Fig. 6a5), which has the longest flight time.

Occasionally, clouds contaminated the measurements, as seen in the leg at 21.32 1 August and 21.30 2 August, for which both the downwelling (Fig. 6) and upwelling
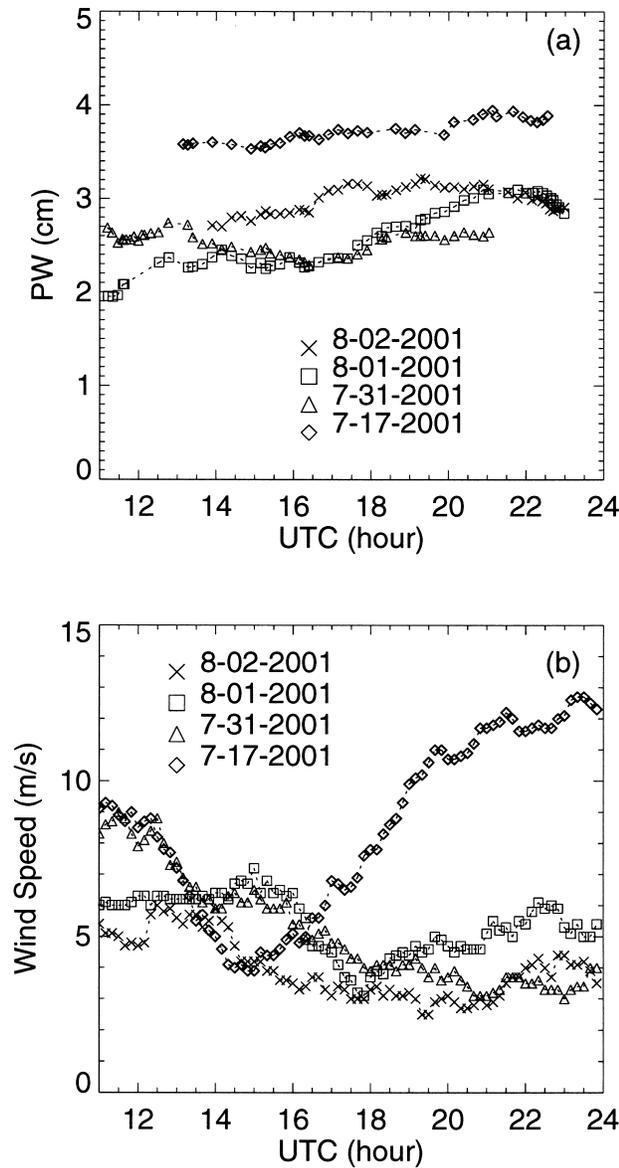
FIG. 2. (a) The total precipitable water and (b) wind speed measured at COVE on the 4 clear days during CLAMS.

FIG. 3. (a) Cimel-measured AOD (500 nm) and (b) SSA (673 nm) of aerosol at COVE on the 4 clear days during CLAMS.

(Fig. 7) fluxes are significantly reduced. Small clouds also affected the surface measurements at COVE around 17.05 1 August and the aircraft measurement for a leg over COVE at this time. There was a cirrus deck observed over the mouth of the bay at around 17.80 17 July that might impact the diffuse field. All model calculations assume clear-sky conditions and use the atmospheric and oceanic properties measured at one single location (COVE) as input, so model results are much smoother than measurements across each entire flight series. Excluding those times with clouds, model–surface differences are within 10 W m^{-2}. The differences between aircraft measurements and surface measurements are somewhat larger (but within 20 W m^{-2}) than
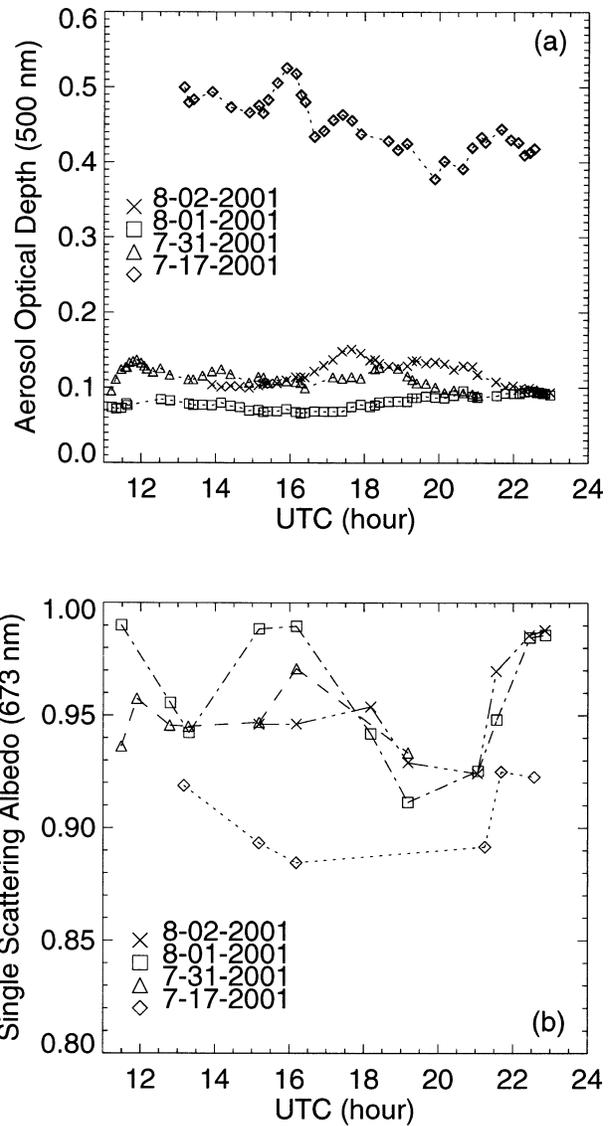
the model–surface differences. Part of these larger differences are due to the aircraft flight height, which is 183 m for most flights. Model simulations for the surface at COVE assume an altitude of 0 m. The downwelling shortwave flux at the 183-m level is about 10 W m^{-2} larger than the surface level on 17 July, when the aerosol was heavy. For the three other days, aerosol loadings are much smaller and the flux differences between 183 m and the surface are much smaller. Another factor, though minor, is the real spatial variance of radiative flux over the flight tracks in Fig. 5. The atmospheric and oceanic conditions differ across each leg. The aircraft and surface-based broadband radiometers were calibrated using procedures established by the Baseline Surface Radiation Network (BSRN; Ohmura et al. 1998), a project of the World Climate Research
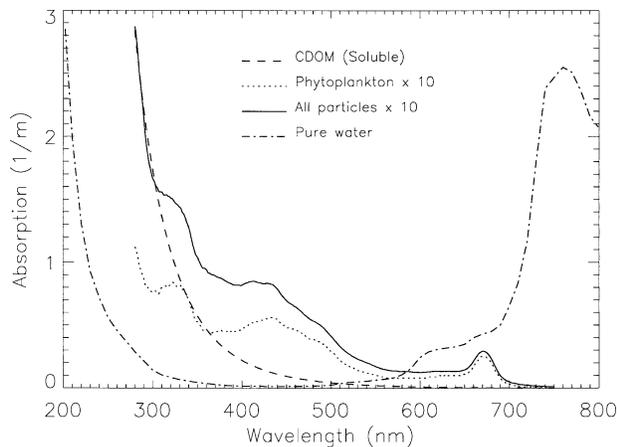
FIG. 4. The average spectral absorption coefficients of ocean materials measured at COVE during CLAMS. The dashed–dotted line is for pure water. Note factor of 10 scale for both curves representing the effects of suspended particulates.

Program (WCRP). The discrepencies shown in Fig. 6 fall within established instrument uncertainties for a global pyranometer (3%–5%).

Figure 7 is similar to Fig. 6, but for the upwelling shortwave fluxes. In Fig. 7, the aircraft-measured upwelling fluxes for the leg around data point 17.9 31 July are substantially larger than other legs in the same flight series. This leg traversed the mouth of the Chesapeake Bay (in the corresponding panel of Fig. 5, the westernmost leg). The water properties at the mouth were different from those under other legs. Specifically, the mouth has more scattering particles (e.g., sediments in the water) that reflect more radiation. This ocean effect will be further explored in a later section. On the same day, the effect of flight altitude on the upwelling flux is also visible in the aircraft data in Fig. 7. The three legs between 17.4 and 17.7 on 31 July are only 31 m above the ocean, lower than the other legs (183 m) in the same flight series. The upwelling fluxes and the differences for the three low-level flights are apparently smaller than other legs in the same flight series due to less atmospheric scattering. Excluding those cloud affected times, most model–surface differences in the upwelling flux are within 2 W m^{-2}, but they are somewhat larger for the time corresponding to the flight 2 in the late afternoon on 2 August, when solar zenith was large and upwelling flux was more sensitive to surface roughness or wind speed. Similar to the downwelling flux, the aircraft–surface differences are also larger than the model–surface differences for most legs. Those factors affected the aircraft downwelling flux and discussed above also affect the upwelling flux measurements and contribute to the discrepancies.

Figure 8 compares the surface-measured (solid lines) and modeled (dashed lines) downwelling and upwelling broadband fluxes and albedo from local noon to near sunset for a mostly clear afternoon of 1 August. Morning

observations of upwelling flux at COVE are not used because of shading by the platform. The dotted lines represent the relative differences between model and measurement. Again, model calculations assume clear-sky conditions and, if cloudy, use aerosol properties measured during the nearest adjacent clear interval. This figure shows that the solar zenith dependences for the downwelling and upwelling fluxes are very different. Unlike the downwelling flux, the surface upwelling flux for clear conditions does not decrease monotonically with solar elevation; there is a peak at around 2200 UTC. This is because the ocean surface albedo increases as solar elevation decreases, and this compensates for the decreased incidence at the surface due to a smaller solar elevation. The relative differences in downwelling flux for clear conditions are within 2%. They are within 10% for upwelling fluxes and albedo. The upwelling flux measured around noon (1700 UTC) is still affected (reduced) by the shadow of the lighthouse frame on the sea. In the late afternoon, the impact of the shadow on the measurement becomes minute, and the measurement noise itself is higher.

Discrepancies between modeled and observed fluxes can be caused by an inadequate radiative transfer model, incorrect inputs to the model, or even observation errors. The aerosol SSA and phase function in the broadband calculations depend on the aerosol model (Hess et al. 1998), because Aeronet SSA and phase function have values at only four wavelengths and are too sparse in temporal coverage. We regard the largest source of model–observation discrepancy for downwelling surface flux to be the inputs for aerosol optical properties in the model. The model error in the downwelling flux will also be transferred to the upwelling flux. Most discrepancies in the upwelling fluxes, however, are likely from incorrect input of ocean optical properties and wind speed. Measurements of ocean optical properties during CLAMS are not as intensive and complete as for the atmospheric properties.

2) COMPARISONS WITH CERES TOA MEASUREMENTS

Terra passed COVE at about 1600 UTC each day during CLAMS. One (of two) CERES instruments was switched to a specially programmed scanning mode that increased the frequency of measurements at COVE by an order of magnitude. Figure 9a compares the CERES directly observed shortwave solar radiances at top of atmosphere (TOA; Wielicki et al. 1996) with those modeled based on the atmospheric and oceanic properties measured in situ at COVE for the 4 clear days during CLAMS. Figure 9b shows the radiance difference between CERES and model versus the TOA radiance. Only those MODIS cloud-screened ocean footprints whose centers were within 15 km of COVE are selected for the comparison (Minnis et al. 2003). View zenith angles range from about 12° to 61°. Many observations
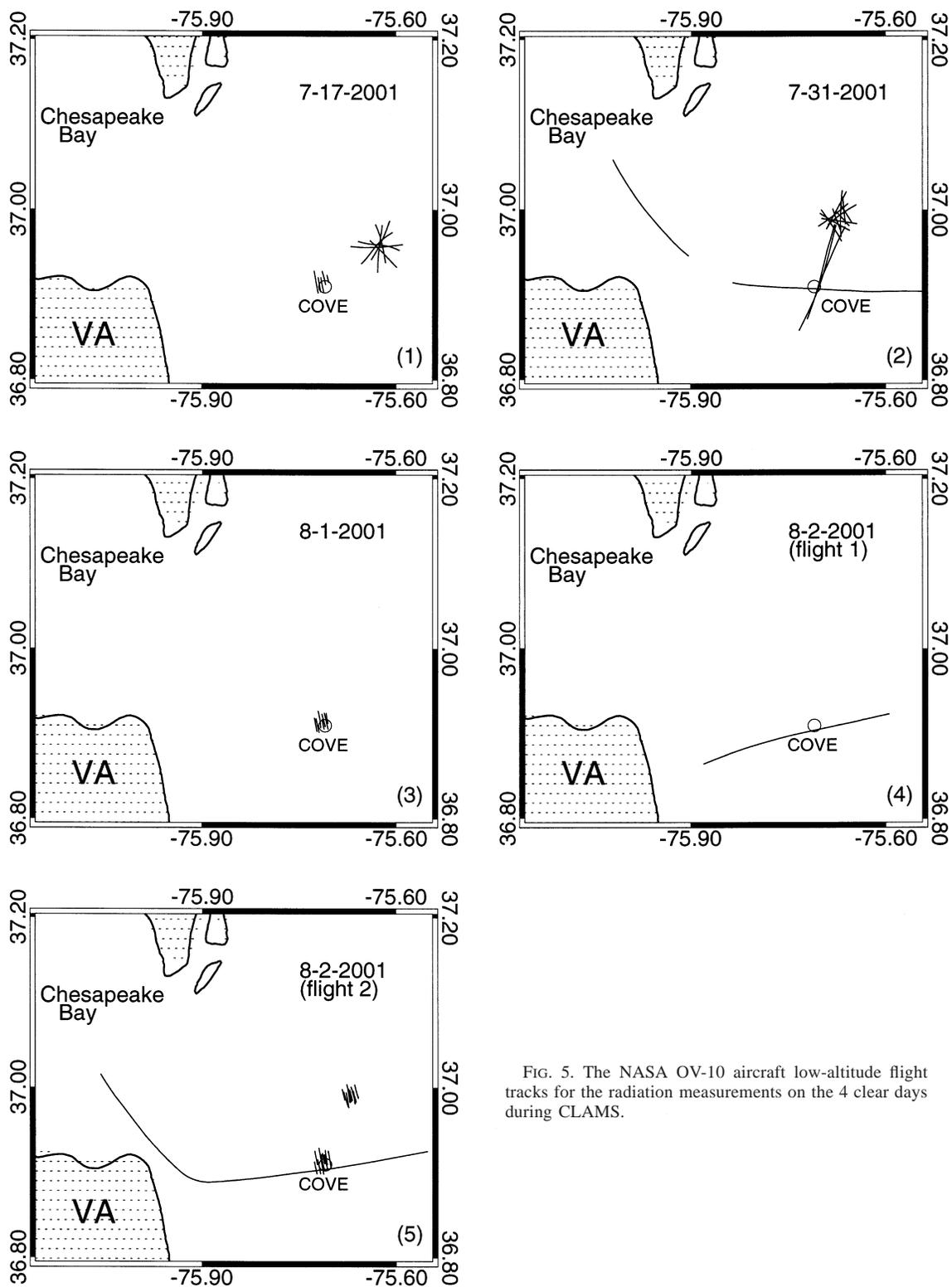
FIG. 5. The NASA OV-10 aircraft low-altitude flight tracks for the radiation measurements on the 4 clear days during CLAMS.
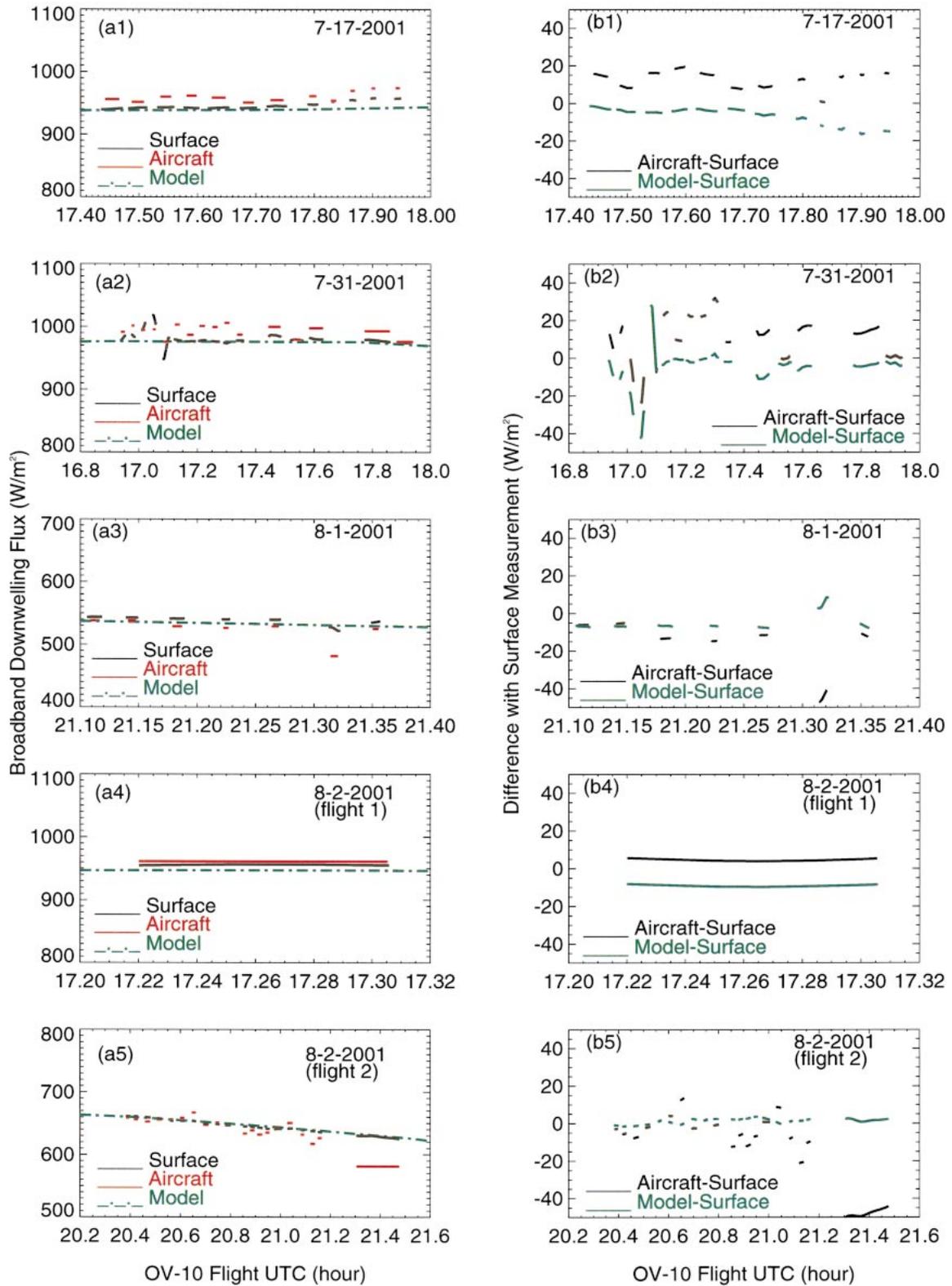
FIG. 6. Comparison of the downwelling shortwave fluxes from surface and aircraft measurements and from model simulations.
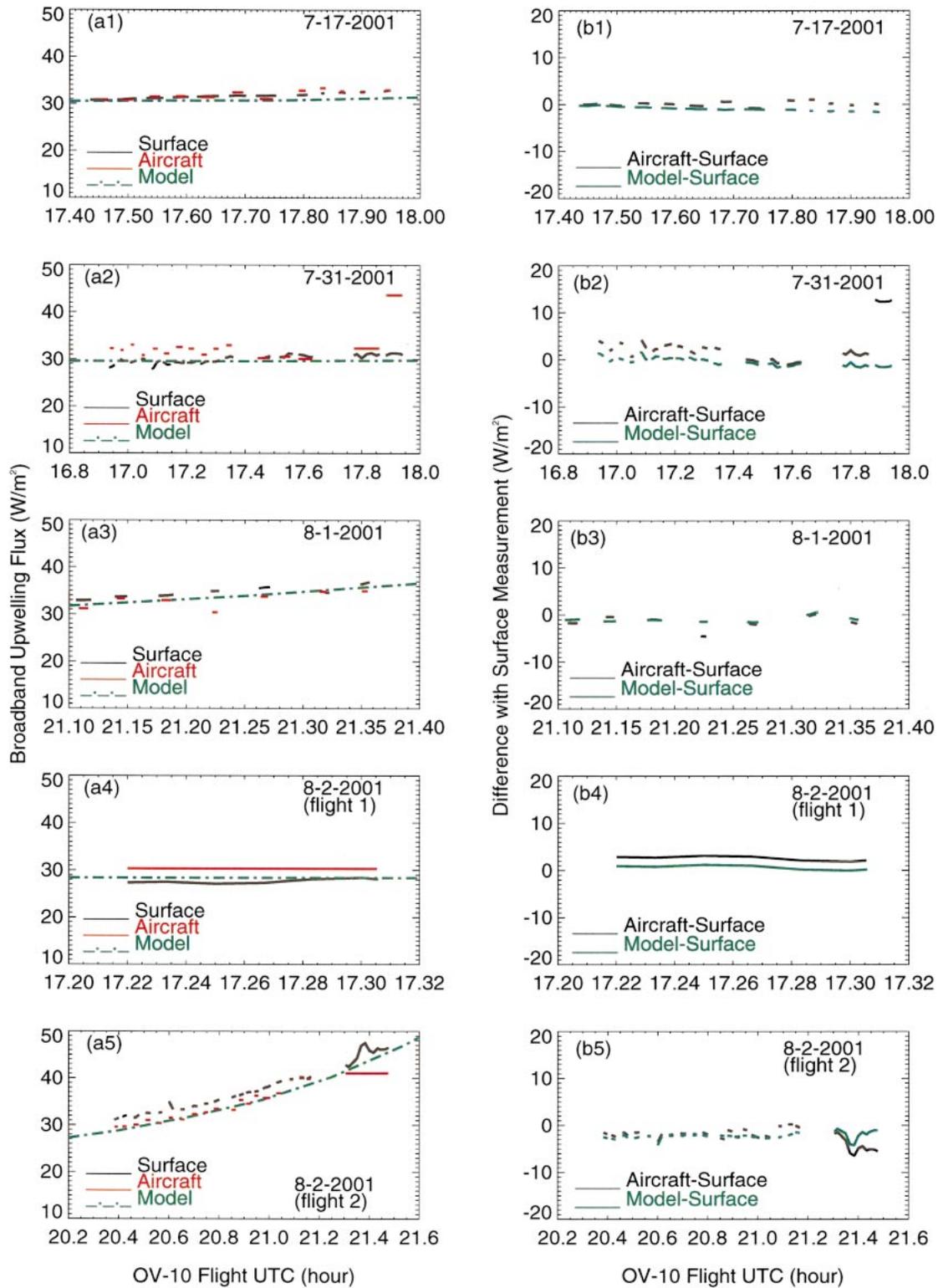
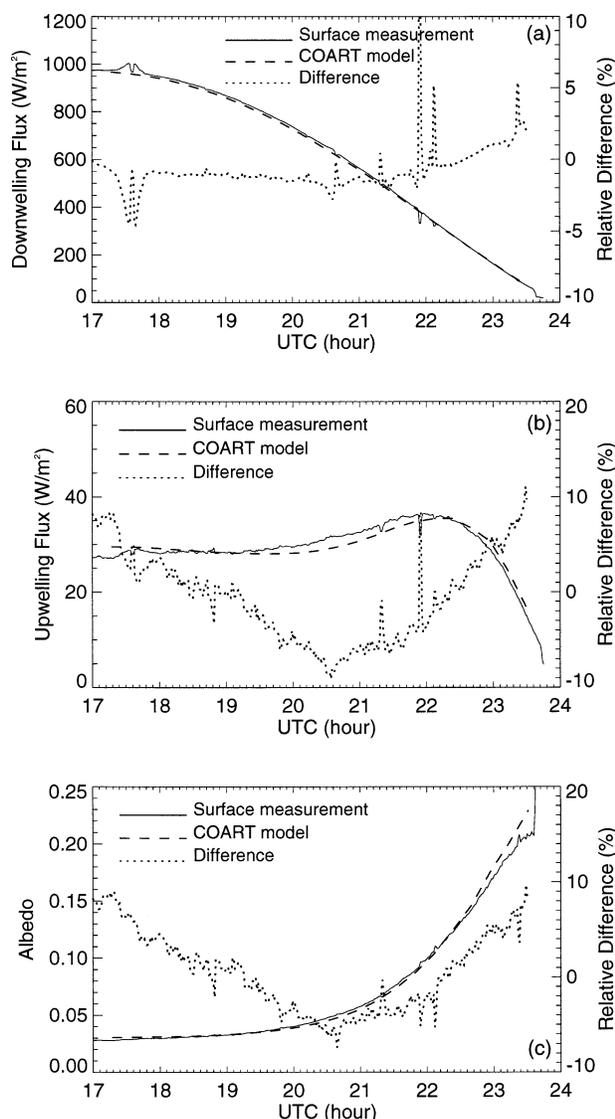FIG. 7. Similar to Fig. 6, but for the upwelling shortwave fluxes.

FIG. 8. Comparison of the surface-measured and COART-modeled (a) downwelling, (b) upwelling shortwave fluxes and (c) ocean surface albedo from local noon to near sunset for the mostly clear afternoon of 1 Aug.
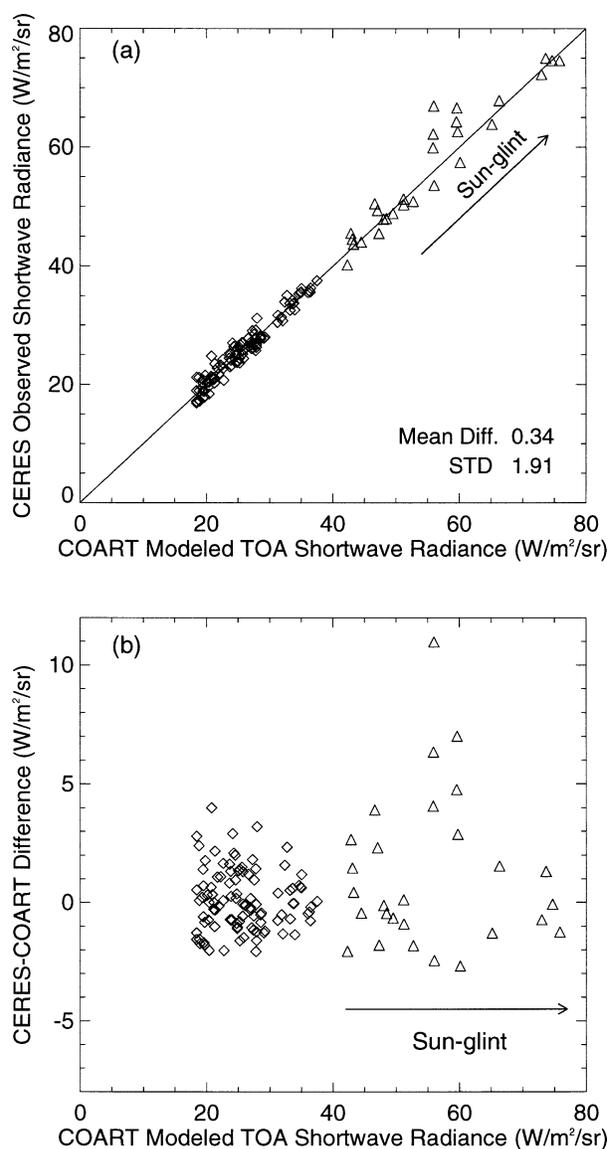

FIG. 9. Comparison of the TOA shortwave solar radiances between (a) the CERES measured and (b) model calculated during the 4 clear days.

fell into the sun-glint region, where the radiances are significantly larger due to specular reflection of the solar beam from the ocean surface. In this glint region, the radiance is very sensitive to the ocean surface conditions or wind speed, and varies sharply with view direction. Therefore, small error in wind speed input may produce a large error in model results. In Fig. 9, the triangles represent those observations whose view direction are within 15° of the specular direction, approximately the center of sun glint. The radiance enhancements in this region are quite appreciable as shown in Fig. 9. The mean difference and the standard deviation (STD) of observation versus model for the whole dataset are 0.34 and 1.91 (W m^{-2} sr^{-1}), respectively (0.51% and 5.9%).

If the radiances within the glint region are excluded, the mean difference and the STD are reduced to 0.11 and 1.27 (W m^{-2} sr^{-1}), respectively (0.16% and 4.9%). The general agreements between CERES observations and model results are good. Any errors in the input atmospheric and oceanic properties would affect this agreement. However, except in sun glint, the uncertainties in the aerosol optical properties used in the model calculations are likely the main source for the discrepancies between observed and computed radiances, because most of the TOA radiances are contributed by atmosphere instead of ocean. For example, the spectral AOD used in the model is based on Cimel observations on a path between COVE and the sun. The AOD from COVE
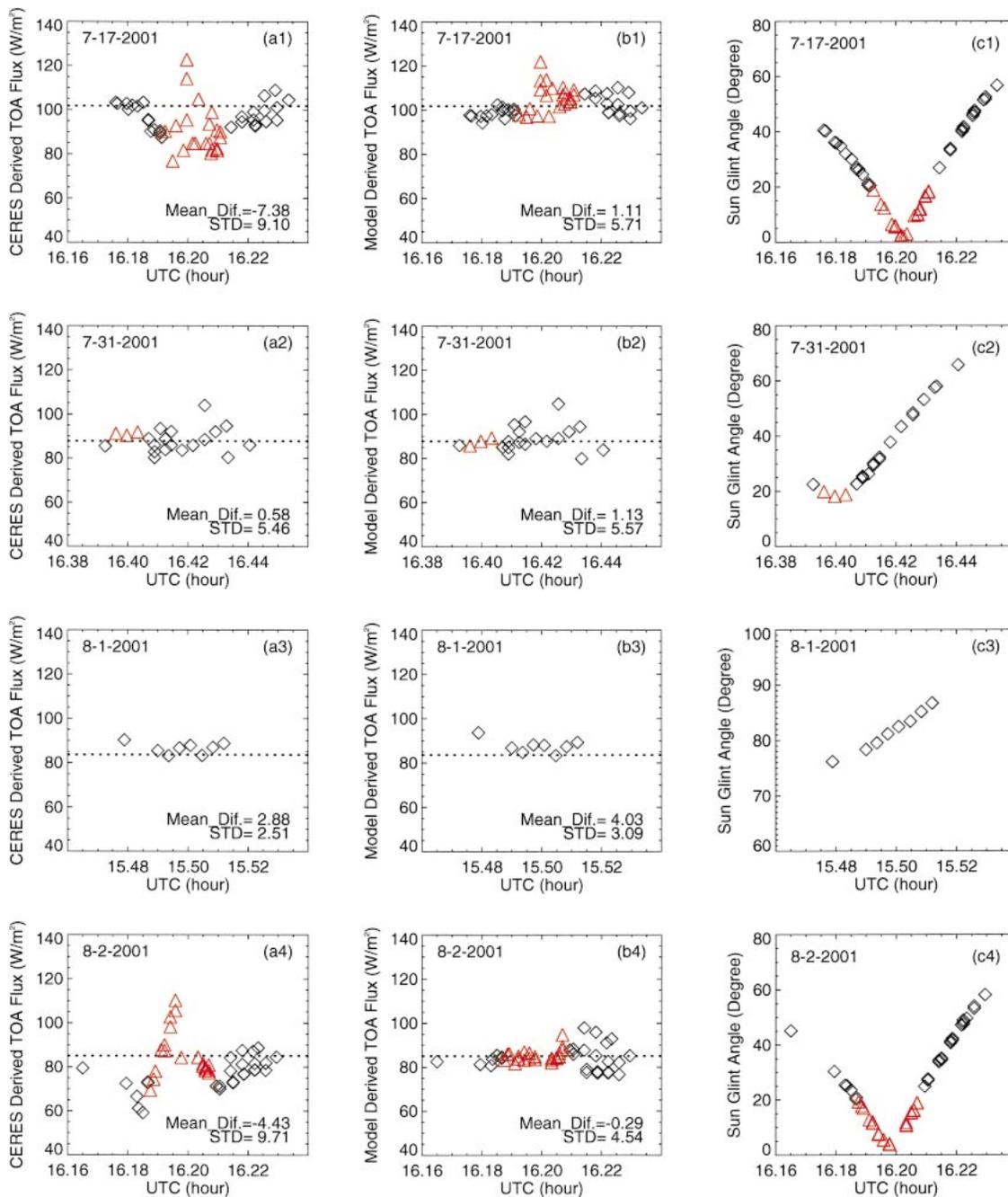
FIG. 10. Comparison of the TOA shortwave upwelling fluxes between CERES and model.

to satellite may be different, especially if the view zenith angle is large, due to potential horizontal variability of aerosol. In addition, aerosol properties measured at COVE are limited to a few individual wavelengths instead of covering the whole solar spectrum as CERES. The different surface coverages in size and location from different view angles also contribute to the differences. Model calculations assume a uniform surface with no clouds. Unscreened clouds would increase observed radiances and fluxes, relative to those modeled.

Figure 10 shows the CERES- and model-derived upwelling TOA fluxes over COVE as a function of CERES measurement time day by day for the 4 clear days in CLAMS. Figures 10a1 to 10a4 are for CERES fluxes, and Figs. 10b1 to 10b4 are for model-derived fluxes. Figures 10c1 to 10c4 show the sun-glint angles for all observations. The sun-glint angle is defined as the angle between the satellite view direction and the specular direction of solar beam. A smaller glint angle corresponds to a larger sun-glint effect. Those observations

with sun-glint angle less than 20° are shown as red triangles in Fig. 10.

Like any other satellite observations, CERES TOA flux must be obtained through the conversion of CERES radiance. CERES TOA fluxes in Figs. 10a1 to 10a4 are estimated from the broadband radiances shown in Fig. 9 by dividing the radiances with anisotropic factors that account for the angular dependence of the radiance. These anisotropic factors are predetermined empirical angular distribution models (ADMs) that are constructed from 9 months of CERES/Tropical Rainfall Measuring Mission (TRMM) cloud-free ocean observations and depend on surface wind speed and aerosol optical depth (Loeb and Kato 2002); the version of CERES *Terra* used here is CER_SSF_Terra-FM2-MODIS_Edition1A. The model-derived fluxes (Figs. 10b1 to 10b4) are also converted from the same CERES-observed radiances through the same procedure used for CERES flux conversion, but use different anisotropic factors. The model-derived fluxes use the anisotropic correction factors from the TOA radiance distribution calculated by COART from the in situ measured atmospheric and oceanic properties. Because no direct TOA flux measurements can be used to compare and check the CERES- or model-derived fluxes converted from radiances, COART is then used to calculate the TOA fluxes again, but here with the usual Gaussian quadrature integration of radiances from discrete ordinates (and corresponding in time to CERES radiance measurements by using those in situ measurements at COVE as input); these fluxes are plotted as dotted lines in Fig. 10. Because constant inputs are used, and the solar zenith angle varies little for a single satellite overpass, the directly calculated TOA fluxes are basically the same in each day. The mean differences between the derived and the COART calculated fluxes, and the STDs of these differences are also shown in Fig. 10. Results in Fig. 10 show that both the CERES- and model-derived fluxes from radiances are distributed around the model-calculated values. The CERES-derived fluxes are similar to the model-derived fluxes on 31 July and 1 August, but CERES fluxes have wider spread on 17 July and 2 August, because many observations are affected by sun glint in these 2 days. When an observation is made in the vicinity of sun glint, the anisotropic factor used for radiance to flux conversion becomes sensitive to wind speed. CERES here uses European Centre for Medium-Range Weather Forecasts (ECMWF) wind speed with four intervals for its ADM. The model-derived fluxes use in situ–measured wind at COVE. The unphysical low fluxes from CERES on 17 July and 2 August are from the observations with small sun-glint angle. They are overcorrected for the anisotropic effect, possibly due to the incorrect wind speeds applied.

For each day, the CERES observations (which specially target COVE at several different view angles in a single pass) were made within a very few minutes; the center of each was within 15 km of COVE; all were

carefully screened for clouds. Ideally, if the atmosphere and ocean were homogeneous horizontally and the ocean state did not vary during the satellite overpass, the TOA fluxes should produce nearly a single value for each overpass. However, it is obvious that the derived TOA fluxes are distributed within a range for each day. There are several factors causing the spread in derived fluxes. One is the inhomogeneity of the actual atmospheric properties, especially aerosol, and the spatial and temporal variation of the oceanic properties, especially the surface condition (e.g., the wind-driven surface roughness). The CERES observations here involve a wide range of view angles, which results in very different footprint sizes and coverages. They cover different areas of coastal waters, which may have different reflectances. Some of them with large view angle may even include small pieces of land in the field of view. Another important factor is error in the anisotropic factor used to convert radiance to flux as described above, especially for those view directions with small sun-glint angle. Though independent ADMs are applied, the variations of the CERES- and model-derived fluxes are similar on 31 July (Figs. 10a2 and 10b2) and on 1 August (Figs. 10a3 and 10b3), in which the sun-glint angles are large for the observations. This indicates that the variability of the fluxes derived from observations with small sun-glint effects is mainly from the actual variation of the radiances observed from different angles due to the inhomogeneity of the atmospheric, surface and oceanic properties.

3) OBSERVED AND MODELED SPECTRAL ALBEDO

Figure 11 shows a comparison between the measured and modeled surface albedo in the six MFRSR channels on 31 July. The solid lines are MFRSR measurements at COVE and the dashed–dotted lines are model results based on the input parameters presented above. The black solid lines represent the measurements (leg average) from the OV-10 aircraft on the flight tracks shown in Fig. 5 (top right) for 31 July. To remove the relative difference between the two instruments and obtain accurate ocean surface albedo, the two surface-based MFRSR instruments used for the downwelling and upwelling irradiance measurements were calibrated relative to each other in advance, by observing the same target at the same time. The mean calibration ratios from these measurements in each channel are applied to the measured albedo calculations of Fig. 11. A similar procedure was also applied to the two field spectrometers aboard the OV-10 and applied to the data presented here.

The rapid variations in MFRSR albedo in Fig. 11 are likely due to changes of the ocean surface (i.e., waves), rather than underlight, because those albedo variations are similar in all the six channels. The aircraft measurements were affected by the flight altitude, the horizontal variability of the atmospheric, surface and oceanic properties, and even the calibration. The three low-
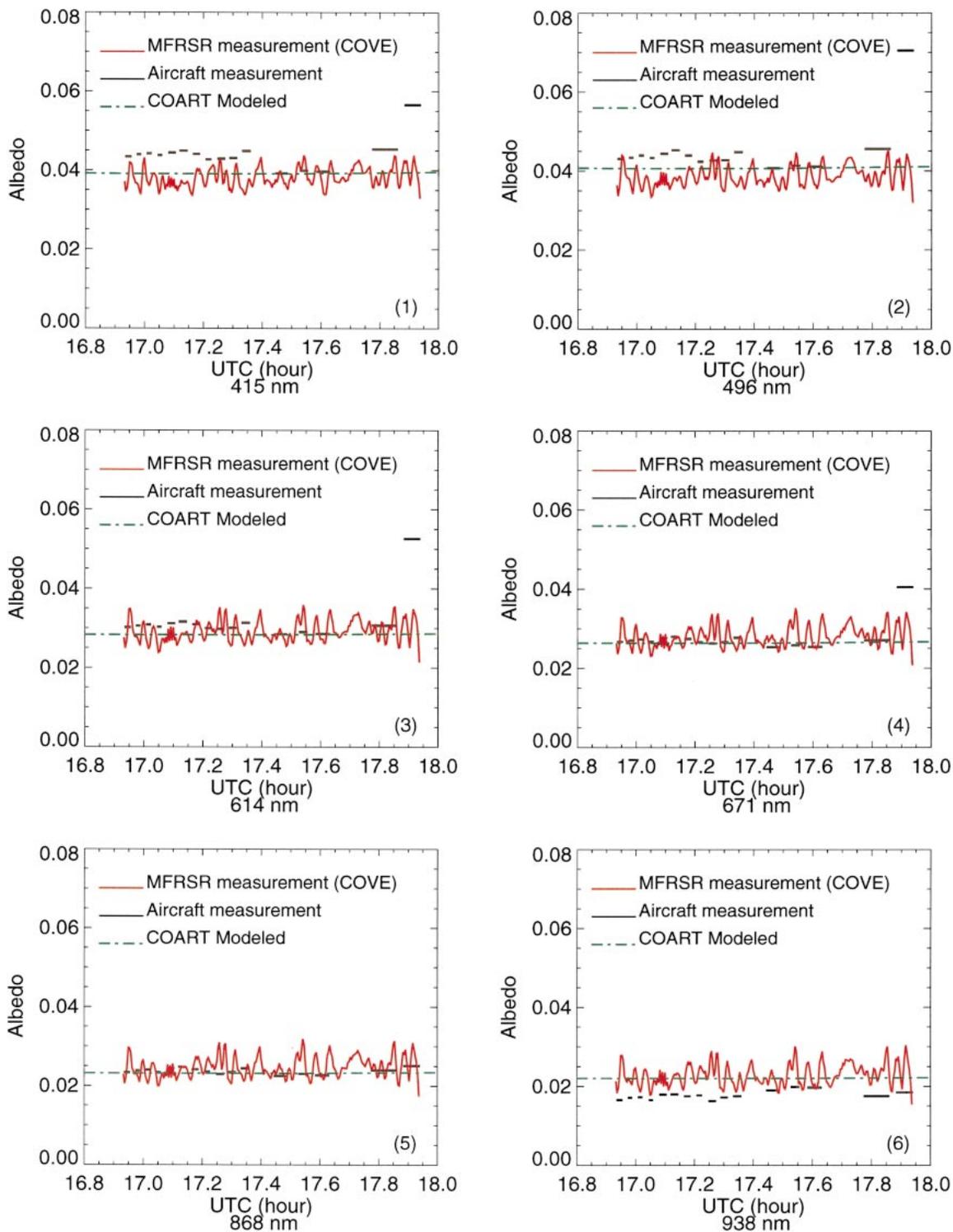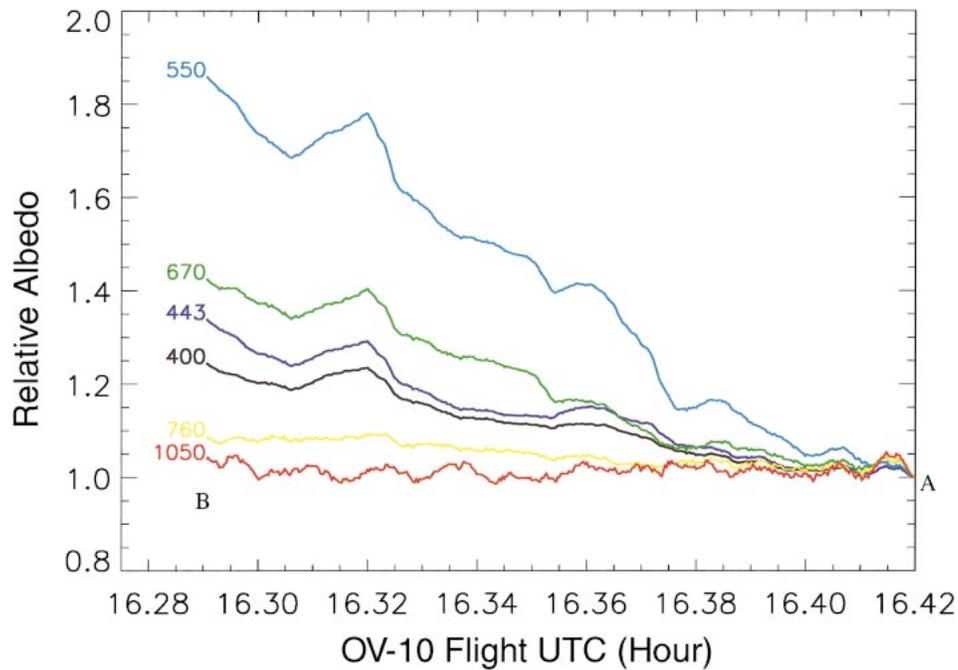
FIG. 11. Comparison of modeled and measured albedo in the six MFRSR channels.

altitude flights (31-m level) between 17.40 and 17.65 show lower albedo in the first five bands but higher albedo in the 938-nm band than other legs with a slightly higher flight altitude (183 m over ocean). This illustrates the significant effect of atmospheric scattering, especially in the first two MFRSR channels (415 and 496 nm), and of water vapor absorption in the sixth channel (938 nm). These scattering/absorption effects are ob-
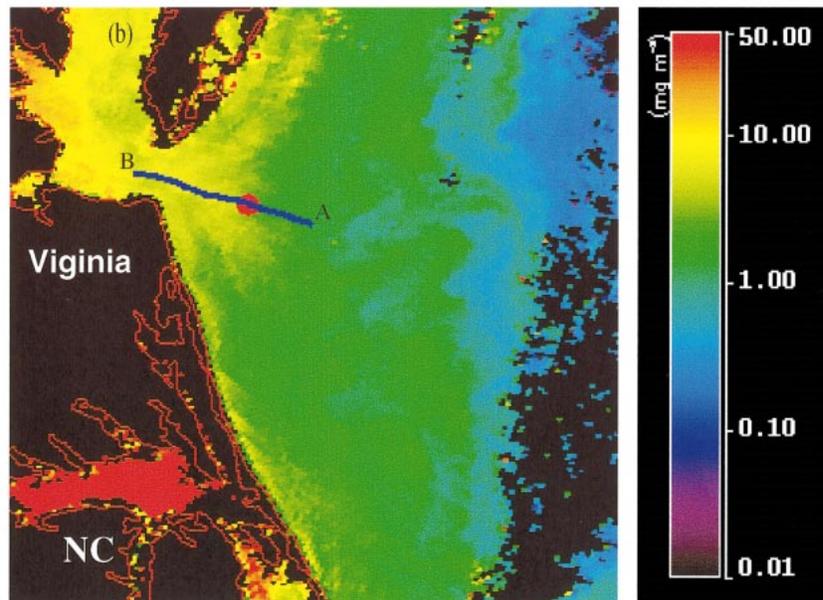
FIG. 12. (a) The aircraft measured albedo at seven wavelengths (b) along a flight track from A to B. Here, (b) is the SeaWiFS chlorophyll image measured 1 h after the aircraft flight.

vious even for mere 150 m of altitude difference in the lower atmosphere. The aircraft data also show significantly higher albedo for the flight leg (the last leg) that traversed across the mouth of the Chesapeake Bay in four of the six channels, especially for the 496-nm channel in which the ocean absorption is small. This supports the hypothesis mentioned above that there were more scattering particle materials in the water there than in the immediate vicinity of COVE. The particles increased the water reflection though the increase is too small to be noticed in the two near-infrared channels because of the strong water absorption in those spectra.

To demonstrate the effect of ocean optics on surface albedo, Fig. 12a shows the albedo variations at six wave-

lengths along a flight from open water beyond COVE to the mouth of the Chesapeake Bay, as shown in Fig. 12b. The flight track (A to B) is overlaid on the chlorophyll concentration image in Fig. 12b. The chlorophyll map is from the Sea-Viewing Wide Field-of-View Sensor (SeaWiFS) measurement at 1732 UTC on the same day, approximately 1 h later than the aircraft flight. The red dot in the image represents COVE. The chlorophyll concentration shows an increase from A to B. All the albedos in Fig. 12a are plotted relative to point A and show different variations from A to B. These different variations for different wavelengths can be explained by the ocean optics. For example, the 550-nm albedo shows the largest increase from A to B, because absorption at this wavelength is small (see Fig. 4 and note effects of phytoplankton particles, CDOM, and water), allowing the increase in particle scattering to have the largest effect on albedo. Chlorophyll absorption is strong at 443 and 670 nm, and this results in smaller increases in albedo from A to B at both wavelengths. At 400 nm, the particle scattering is largest, has little absorption by water, and even less chlorophyll absorption than does 443 nm, but as CDOM absorption decreases exponentially with wavelength, the increase in albedo at 400 nm (from A to B) is yet lower than at 443, 550, or 670 nm. Due to the large absorption by sea water, the 760-nm albedo has only a slight increase from A to B. The water absorption at 1050 nm is so strong that the albedo at this wavelength is insensitive to the ocean optical properties. The albedo at 1050 nm is determined by the surface conditions and shows different variations along the flight track from other wavelengths. It should be noted that the phytoplankton particles are not solely responsible for the variations of the ocean optics here, and therefore, the chlorophyll is not the only factor affecting the albedo variations from A to B. Figure 11 demonstrates the significant impact of subsurface ocean optical properties on ocean surface albedo.

Spectral albedos measured at COVE, observed from aircraft, and simulated by the model were all compared for high sun on 31 July in Fig. 11. We now consider spectral albedos on 31 July from local noon to sunset using measurements at COVE and the model (but not the aircraft). Figure 13 compares measured and modeled albedo in the six MFRSR channels for 31 July (results for 1 August were similar and are not shown). In Fig. 13, the solid lines represent the MFRSR measurements; the dashed lines are for model results; and the dashed–dotted lines are for the relative differences between model and surface measurement. Both the model and observation results show that the reflectances and their dependence on time or sun elevation are different from channel to channel. For example, due to the larger aerosol effect, the reflectance in channel 1 increases first, then decreases as solar elevation decreases, while the reflectances in the other channels basically increase monotonically with solar zenith angle. But sensitivity to solar angle varies among the channels because aerosol effects and atmospheric transmissions are different in the different MFRSR channels. Except in the late afternoon, the relative model–observation difference is within 10% for MFRSR channels 1 and 2, but larger in other channels. The larger differences in the late afternoon are due to the increasing instrument noise at low-energy level.

4) COMPARISONS WITH AIRMISR

In CLAMS, upwelling radiances were measured by AirMISR aboard the NASA ER-2 aircraft at 20 km above the surface. Two of the measurements were over the ocean by COVE in 2 clear days (17 July and 2 August). Figure 14 shows the measured (asterisk) and modeled (diamond) equivalent reflectances (Kahn et al. 2001) versus view angle for the four AirMISR spectral channels on 17 July (Figs. 14a1 to 14a4) and on 2 August (Figs. 14b1 to 14b4); DF to DA represent the nine view angles of MISR on *Terra* (Diner et al. 1998). The view geometry specifications and the sun-glint angles for the observations are listed in Table 1. These observations cover a wide range of view angles from backscattering to forward-scattering directions. As shown in Table 1, the view directions AF and AN on 17 July have the smallest sun-glint angles, for which we expect the largest impact of specular reflection by the ocean surface. This sun-glint effect can be seen in the reflectances shown in Fig. 14. The sun-glint effect on 17 July is marginal in the blue channel due to blurring from strong scattering by atmospheric molecules and aerosol, but it becomes successively more apparent from the green channel to the near-infrared (NIR) channel as atmospheric scattering decreases. This is similar for the measurements on 2 August, but the largest sun-glint-affected directions are AA and AN on this day. The aerosol effect on the sun glint is also notable: sun glint is more apparent in the right panels for 2 August (which had less aerosol) than in the left panels for 17 July (which had more aerosol). At angles away from sun-glint peak, the larger aerosol loading on 17 July resulted in much higher reflectance than on 2 August, especially in the red and NIR channels.

Coincident with the AirMISR measurements, the NASA AATS-14 on board the Convair-580 aircraft measured AOD from below the ER-2 aircraft. These AOD data have been used in the model calculations for Fig. 14 (but not in earlier figures). The AATS-14 AOD is slightly higher than the surface-based AERONET Cimel AOD in the near infrared. Like the irradiance, the radiance is also sensitive to the AOD, SSA and asymmetry factor of aerosol. But unlike the irradiance, the directional radiance distribution or the angular pattern is quite sensitive to the aerosol scattering phase function, and hence, the commonly used Henyey–Greenstein phase function, which is represented by the asymmetry factor and is usually adequate for irradiance calculations, is
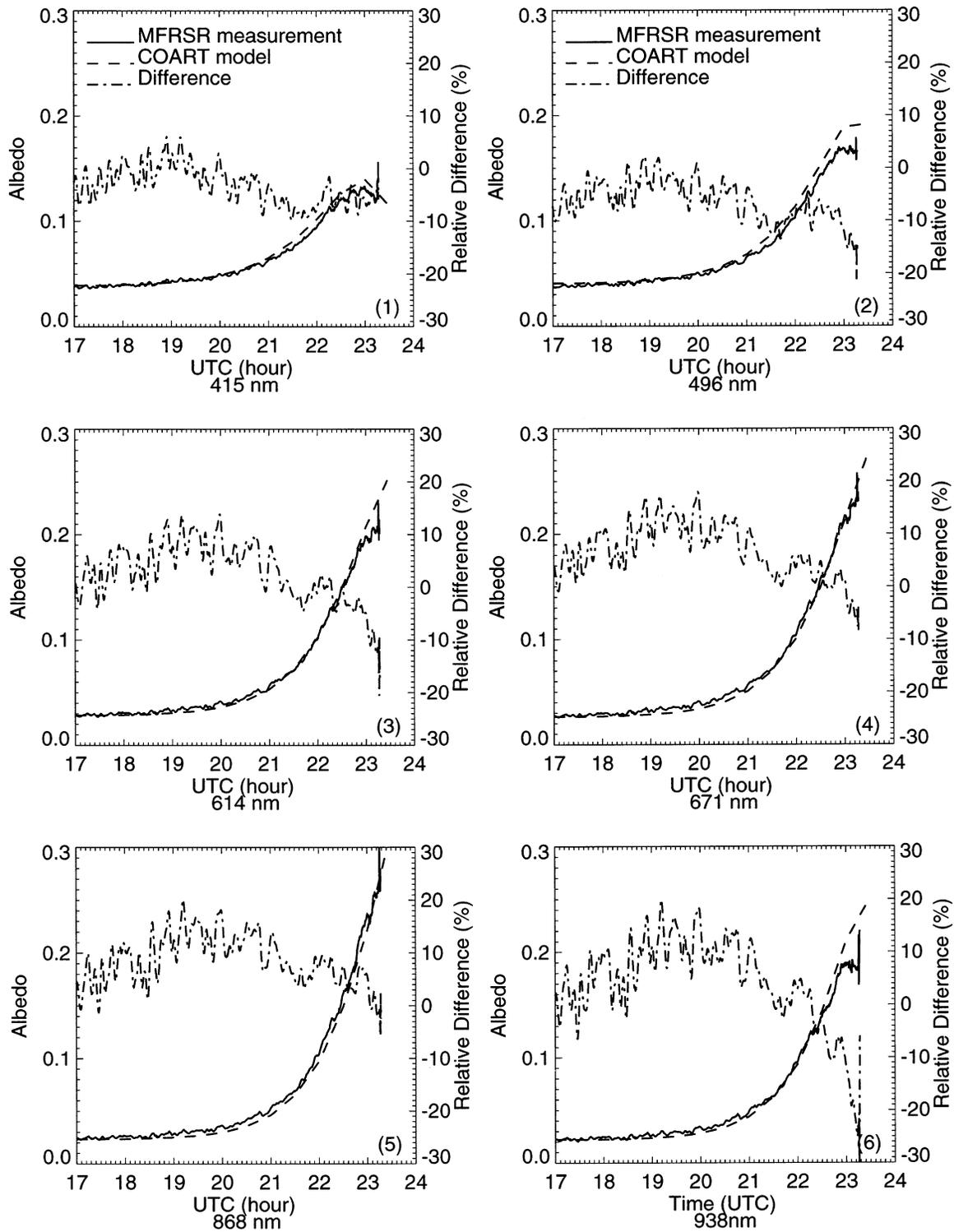
FIG. 13. Comparison of the measured and modeled MFRSR albedo from noon to near sunset on 31 Jul 2001.

not adequate for model simulations here. An actual full phase function has to be used to obtain a good model-observation agreement here. In other words, everything in the aerosol optical properties, including the phase

function must be right to obtain the correct radiances at all the very different directions as MISR. While the overall magnitude of the MISR reflectance is sensitive to AOD and SSA, its angular pattern is mainly deter-
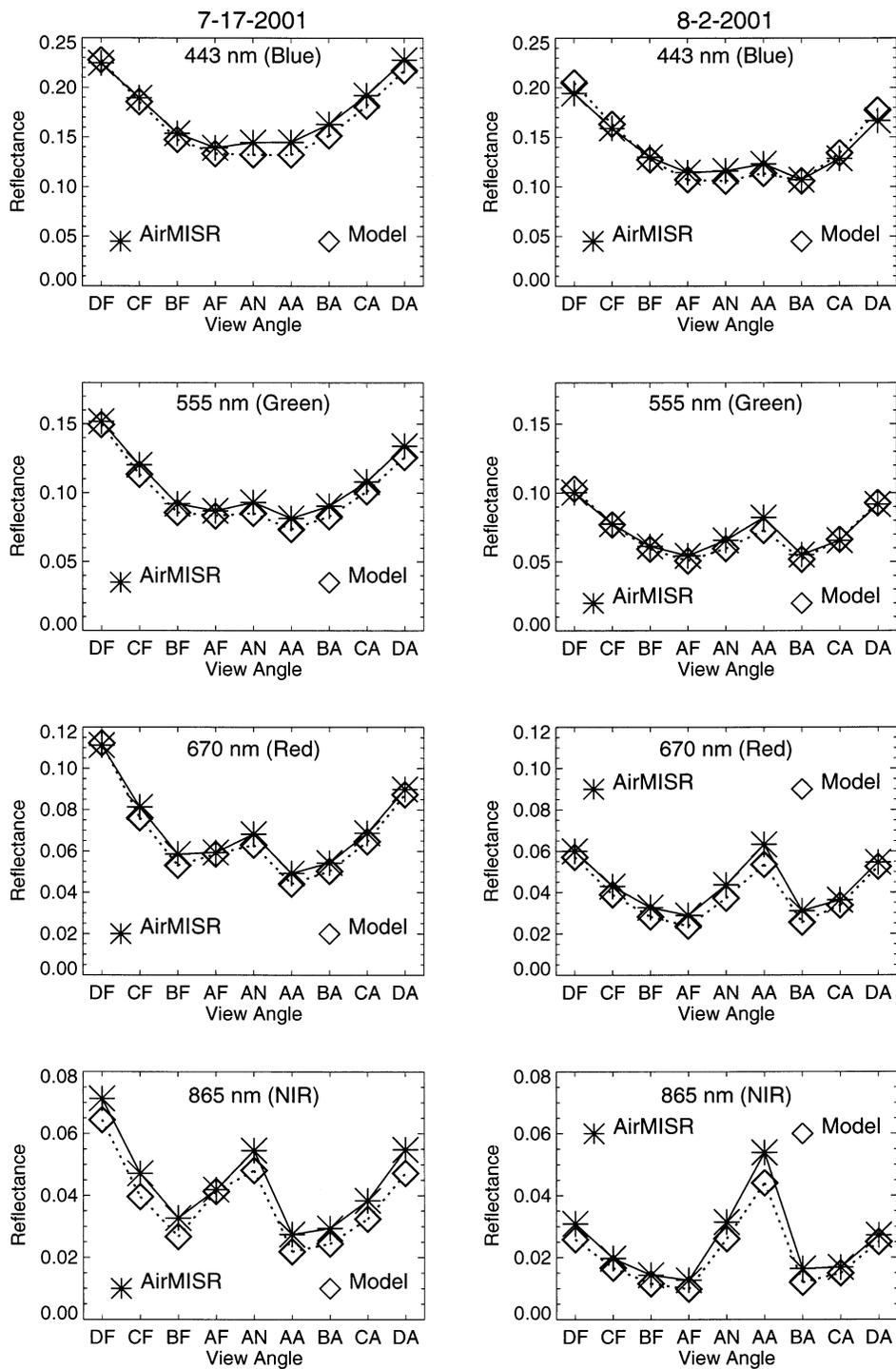
FIG. 14. Comparison of AirMISR-measured and model-simulated reflectances in the four spectral bands at 20 km above surface on 17 Jul during CLAMS.

mined by the scattering phase function, which is closely related to the aerosol size distribution. Because of these sensitivities of the upwelling radiances and their angular distribution at high altitudes to the aerosol input parameters in the model calculations, the multiangle AirMISR

data provides a good database for checking the quality of aerosol properties either measured or retrieved.

Based on Fig. 14, the directional distribution patterns of measurement and model radiance are very similar, including that in the sun glint. View direction DF on

TABLE 1. AirMISR view geometry.

View angle	Sun zenith		View zenith		Relative azimuth		Sun-glint angle	
	17 Jul	2 Aug	17 Jul	2 Aug	17 Jul	2 Aug	17 Jul	2 Aug
DF	20.5	23.4	71.2	74.3	301.5	128.7	61.6	89.5
CF	20.2	23.2	61.0	65.4	301.6	129.6	52.2	81.1
BF	20.1	23.0	46.3	50.8	300.5	130.6	39.3	67.3
AF	20.0	22.9	26.9	31.0	296.4	131.2	24.9	48.9
AN	19.9	22.8	4.6	2.0	225.0	140.9	23.3	24.4
AA	19.8	22.7	25.6	26.7	135.4	310.9	41.9	20.3
BA	19.7	22.6	44.9	46.8	131.1	311.7	59.3	35.0
CA	19.5	22.5	59.5	60.9	129.9	312.4	73.0	47.6
DA	19.3	22.3	70.3	71.0	129.9	313.4	83.2	56.8

17 July and DA on 2 August are closest to the forward scattering direction on each day. In these view angles, the modeled reflectances are higher than or closer to the measurements, indicating the phase functions used here might have a little too much forward scattering, that might result from the larger than actual aerosol size. Except for the forward scattering direction (i.e., DF), the modeled reflectances on 17 July are lower than the AirMISR measurements, probably because the SSA used is a little too low. The AERONET-retrieved aerosol SSA and phase function are used in the model calculations here.

5. Conclusions

The comprehensive observations on the radiation and the ancillary physical and optical properties for atmosphere and ocean obtained in the CLAMS experiment provide an excellent database for validation of radiative transfer models and remote sensing retrieval algorithms. Radiation measurements from the lighthouse tower, aircraft, and space over the ocean in the 4 clear days during CLAMS are analyzed with the coupled radiative transfer model (COART). The model is successively compared with observations of broadband fluxes and albedos near the ocean surface from the COVE sea platform and a low-level OV-10 aircraft, of near-surface spectral albedos from COVE and OV-10, of broadband radiances at multiple angles and inferred TOA fluxes from CERES, and of spectral radiances at multiple angles from AirMISR at 20-km altitude. The results show that the radiation measurements from different platforms are consistent with each other and with radiative transfer modeling.

Clear-sky model–observation discrepancies for downwelling shortwave flux at surface are within 10 W m^{-2}. In most cases, model–observation discrepancies for upwelling shortwave flux at surface are within 2 W m^{-2}. The model–observation discrepancies for shortwave ocean albedo are less than 8%; some discrepancies in spectral albedo are larger but less than 20%. The discrepancies between low-altitude aircraft and surface measurements are somewhat larger than those between the model and the surface measurements; the former are

due to the effects of differences in height, aircraft pitch and roll, and the noise of spatial and temporal variations of atmospheric, surface and oceanic properties. CERES radiances at TOA and AirMISR radiances at 20 km above the surface can also be well simulated by the coupled radiative transfer model, but CERES TOA fluxes can vary significantly from model calculations for the sun-glint affected observations. The spatial inhomogeneity of the atmosphere and ocean have impacted the CERES observations for the same target from different angles, and hence, the CERES fluxes inferred from the radiances.

The intercomparison among measurements from different platforms and the model show that at the surface, the uncertainties of aerosol properties are the main error source for the modeled downwelling fluxes; while the uncertainties of ocean surface model and ocean optical properties are the main error source for the modeled upwelling fluxes. Atmospheric scattering significantly affects the radiation in the lower atmospheric layers, especially in shortwave spectra. At the TOA and at high altitudes, the model–observation discrepancies in the spectral and broadband upwelling radiances are mainly from the uncertainties of the surface and aerosol properties, including their horizontal variability. The multiple angle AirMISR observations also indicate the importance of aerosol scattering phase function on the upwelling radiances in the upper atmosphere. In addition to the uncertainties of aerosol and ocean properties, the anisotropic correction error also affects the CERES TOA flux, especially for the observations affected by the sun glint.

The model–observation agreements prove that most of the observational data in CLAMS are robust, and the coupled atmosphere–ocean radiative transfer model correctly treats the scattering and absorption processes in both the air and water. The validated data and model can be used to check, develop, and improve retrieval algorithms for radiation and aerosol properties from satellite data.

AERONET data. David Ruble, Xiaoju Pan, and Jian Wang collected the oceanographic observations.

REFERENCES

Charlock, T. P., and T. L. Alberta, 1996: The CERES/ARM/GEWEX Experiment (CAGEX) for the retrieval of radiative fluxes with satellite data. *Bull. Amer. Meteor. Soc.,* **77,** 2673–2683.

Cox, C., and W. Munk, 1954: Measurement of the roughness of the sea surface from photographs of the sun's glitter. *J. Opt. Soc. Amer.,* **44,** 838–850.

Diner, D. J., and Coauthors, 1998: The Airborne Multi-angle Imaging SpectroRadiometer (AirMISR): Instrument description and first results. *IEEE Trans. Geosci. Remote Sens.,* **36,** 1339–1349.

Dubovik, O., and M. D. King, 2000: A flexible inversion algorithm for retrieval of aerosol optical properties from sun and sky radiance measurements. *J. Geophys. Res.,* **105,** 20 673–20 696.

Hess, M., P. Koepke, and I. Schult, 1998: Optical properties of aerosols and clouds: The software package OPAC. *Bull. Amer. Meteor. Soc.,* **79,** 831–844.

Holben, B. N., and Coauthors, 1998: AERONET—A federated instrument network and data archive for aerosol characterization. *Remote Sens. Environ.,* **66,** 1–16.

Jin, Z., and K. Stamnes, 1994: Radiative transfer in nonuniformly refracting layered media: Atmosphere–ocean system. *Appl. Opt.,* **33,** 431–442.

——, T. P. Charlock, K. Rutledge, 2002: Analysis of broadband solar radiation and albedo over the ocean surface at COVE. *J. Atmos. Oceanic Technol.,* **19,** 1585–1601.

Kahn, R., P. Banerjee, D. McDonald, and J. Martonchik, 2001: Aerosol properties derived from aircraft multi-angle imaging over Monterey Bay. *J. Geophys. Res.,* **106,** 11 977–11 995.

Kato, S., T. P. Ackerman, J. H. Mather, and E. E. Clothiaux, 1999: The K-distribution method and correlated-k approximation for a shortwave radiative transfer Model. *J. Quant. Spectros. Radiat. Trans.,* **62,** 109–121.

Loeb, N. G., and S. Kato, 2002: Top-of-atmosphere direct radiative effect of aerosol over the tropical oceans from the Clouds and the Earth's Radiant Energy System (CERES) satellite instrument. *J. Climate,* **15,** 1474–1484.

Minnis, P., D. F. Young, S. Sun-Mack, P. W. Heck, D. R. Doelling, and Q. Trepte, 2003: CERES Cloud Property Retrievals from Imagers on TRMM, Terra, and Aqua. *Proc. SPIE 10th Int. Symp. on Remote Sensing: Conf. on Remote Sensing of Clouds and the Atmosphere VII,* Barcelona, Spain, International Society for Optical Engineering, 37–48.

Mobley, C., and Coauthors, 1993: Comparison of numerical models for computing underwater light fields. *Appl. Opt.,* **32,** 7484–7504.

Morel, A., 1991: Light and marine photosynthesis: A spectral model with geochemical and climatological implications. *Progress in Oceanography,* Vol. 26, Pergamon, 263–306.

Ohmura, A., and Coauthors, 1998: Baseline Surface Radiation Network (BSRN/WCRP): New precision radiometry for climate research. *Bull. Amer. Meteor. Soc.,* **79,** 2115–2136.

Redemann, J., and Coauthors, 2005: Suborbital measurements of spectral aerosol optical depth and its variability at subsatellite grid scales in support of CLAMS, 200. *J. Atmos. Sci.,* **62,** 993–1007.

Smith, W. L., Jr., T. P. Charlock, R. Kahn, J. V. Martins, L. A. Remer, P. V. Hobbs, J. Redemann, and C. K. Rutledge, 2005: EOS *TERRA* aerosol and radiative flux validation: An overview of the Chesapeake Lighthouse and Aircraft Measurements for Satellites (CLAMS) experiment. *J. Atmos. Sci.,* **62,** 903–918.

Stamnes, K., S. C. Tsay, W. J. Wiscombe, and K. Jayaweera, 1988: Numerically stable algorithm for discrete-ordinate-method radiative transfer in multiple scattering and emitting layered media. *Appl. Opt.,* **27,** 2502–2509.

Wielicki, B. A., B. R. Barkstrom, E. F. Harrison, R. B. Lee, G. L. Smith, and J. E. Cooper, 1996: Clouds and the Earth's Radiant Energy System (CERES): An Earth Observing System experiment. *Bull. Amer. Meteor. Soc.,* **77,** 853–868.